






Multiple Sub-Pixel Target Detection for Hyperspectral Imaging Systems

Pia Addabbo , Senior Member, IEEE, Nicomino Fiscante, Student Member, IEEE, Gaetano Giunta , Senior Member, IEEE, Danilo Orlando , Senior Member, IEEE, Giuseppe Ricci , Senior Member, IEEE, and Silvia Liberata Ullo , Senior Member, IEEE

Abstract—Hyperspectral target detection is a task of primary importance in remote sensing since it allows for location and discrimination of target features. To this end, the reflectance maps, which contain the spectral signatures and related abundances of the materials in the observed scene, are often used. However, due to the low spatial resolution of most hyperspectral sensors, targets occupy a fraction of the pixel and, hence, the spectra of different sub-pixel targets (including the background spectrum) are mixed together within the same pixel. To solve this issue, in this paper, we adopt a generalized replacement model accounting for multiple sub-pixel target spectra and formulate the detection problem at hand as a binary hypothesis test where under the alternative hypothesis the target is modeled in terms of a linear combination of endmembers whose coefficients also account for the presence of the background. Then, we devise detection architectures based upon the generalized likelihood ratio test where the unknown parameters are suitably estimated through procedures inspired by the maximum likelihood approach. The performances of the proposed decision schemes are evaluated by means of both synthetic as well as real data and compared with other counterparts by showing the effectiveness of the proposed procedure.

Index Terms—Detection, generalized likelihood ratio test, hyperspectral imaging, maximum likelihood estimation, sub-pixel target.

NOTATION AND ACRONYMS

In what follows, vectors and matrices are denoted by boldface lower-case and upper-case letters, respectively. Symbols $\det(\cdot)$ and $\text{Tr}(\cdot)$ denote the determinant and the trace of a square matrix, respectively. Symbols \mathbf{I} and $\mathbf{0}$ represent the identity matrix and the null vector or matrix of suitable dimensions, respectively. $\mathbf{1}$ is the vector of ones. As to the numerical sets, \mathbb{R} is the set of real numbers, $\mathbb{R}^{N \times M}$ is the Euclidean space of $(N \times M)$ -dimensional real matrices (or vectors if $M = 1$). We use $(\cdot)^T$ to

denote the transpose while $\|\cdot\|$ is the Euclidean norm of a vector. We write $\mathbf{x} \sim \mathcal{N}_N(\boldsymbol{\mu}, \mathbf{M})$ if \mathbf{x} is a N -dimensional Gaussian vector with mean $\boldsymbol{\mu} \in \mathbb{R}^{N \times 1}$ and positive definite covariance matrix $\mathbf{M} \in \mathbb{R}^{N \times N}$.

Finally, we provide below a list of the used acronyms:

ACE	Adaptive Coherence Estimator.
ACUTE	Adaptive Cell Under Test Estimator.
AMF	Adaptive Matched Filter.
ASD	Adaptive Subspace Detector.
GLRT	Generalized Likelihood Ratio Test.
MC	Monte Carlo.
MLE	Maximum Likelihood Estimate.
MSD	Matched Subspace Detector.
OSP	Orthogonal Sub-space Projection.
PDF	Probability Density Function.
PUT	Pixel Under Test.
RIT	Rochester Institute of Technology.
RMS	Root Mean Square.
RMSE	Root Mean Square Error.
SMF	Spectral Matched Filter.

I. INTRODUCTION

HYPERSPECTRAL imaging spectrometers enable the detection and discrimination of different target features in a scene due to hundreds or thousands of spectral channels covering the visible, near and shortwave infrared and ultraviolet spectral bands. Their field of application is very wide and ranges from agricultural remote sensing, object classification, atmospheric monitoring, to military investigation [1], [2], [3], [4].

On the other hand, the consequent low spatial resolution entails a challenging situation due to the fact that different materials can jointly occupy a single Pixel Under Test (PUT). As a matter of fact, the spectra of different sub-pixel targets (including the background spectrum) are mixed together as well as the corresponding fraction (or abundance) of constituent endmembers. In general, the number of endmembers and their abundances at each pixel are unknowns and the corresponding estimation process, i.e., the hyperspectral unmixing, gets complicated due to the model inaccuracies, the observation noise, the environmental conditions, and the endmember variability [5].

Unmixing algorithms currently rely on mixing models that can be either linear or nonlinear. The first case corresponds to a macroscopic mixing scale, whereas the second one is more representative of the physical interactions between the scattering from multiple materials. As for the unmixing methods, signal-subspace, geometrical, statistical, sparsity-based, and

Manuscript received 15 November 2022; revised 24 February 2023; accepted 1 April 2023. Date of publication 13 April 2023; date of current version 11 May 2023. The associate editor coordinating the review of this manuscript and approving it for publication was Dr. Monica F. Bugallo. (*Corresponding author: Silvia Liberata Ullo.*)

Pia Addabbo is with the Università degli Studi “Giustino Fortunato”, 82100 Benevento, Italy (e-mail: piaaddabbo@gmail.com).

Nicomino Fiscante and Gaetano Giunta are with the Industrial, Electronic and Mechanical Engineering Department, University of Roma Tre, 00146 Rome, Italy (e-mail: Nicomino.fiscante@uniroma3.it; gaetano.giunta@uniroma3.it).

Danilo Orlando is with the Università degli Studi “Niccolò Cusano”, 00166 Roma, Italy (e-mail: danilor78@gmail.com).

Giuseppe Ricci is with the Dipartimento di Ingegneria dell’Innovazione, Università del Salento, 73100 Lecce, Italy (e-mail: giuseppe.ricci@unisalento.it).

Silvia Liberata Ullo is with the University of Sannio, 82100 Benevento, Italy (e-mail: ullo@unisannio.it).

Digital Object Identifier 10.1109/TSP.2023.3265890

spatial-contextual procedures have been proposed over the years [6].

Recent advances, in the field of hyperspectral imaging, are directed towards the development of target detection algorithms fed by hyperspectral images and exploiting spectral signatures of the materials to identify the targets of interest [7]. In this case, the separation of the background signature from the desired targets represents the major challenge and the actual classification procedures are not directly applicable to target detection since the targets' number is typically too small for using clustering-based algorithms. Moreover, the targets of interest may appear as sub-pixel targets where the background interference directly distorts the shape of the real observed target spectrum.

With reference to this latter issue, different solutions have been proposed for target detection in hyperspectral imaging [8]. The main difference between the various algorithms relies on the availability of prior knowledge about the spectral characteristics of the desired targets. When the target spectral information is not a-priori known, or is affected by uncertainty, anomaly detectors can be used, where hyperspectral image anomalies are related to a general kind of spectral irregularity due to the presence of atypical objects. In this case, pattern recognition or statistical schemes are used for the detection of the objects that stand out from the background [9]. On the contrary, if the spectral characteristics of the desired targets are a-priori known, both the noise and the background can be statistically modeled as Gaussian-distributed and several classical target detection algorithms can be used, such as the linear Spectral Matched Filter (SMF), the Matched Subspace Detector (MSD), the Adaptive Subspace Detector (ASD), and the Orthogonal Sub-space Projection (OSP) [10]. However, these detectors do not consider any constraint on the abundance of sub-pixel targets and background. Otherwise stated, they do not account for the fact that when a sub-pixel target is present, the amount of background should be reduced by the same proportion, which leads to the definition of the so called *replacement model*, by which a sub-pixel target is supposed to "replace" or fill part of the background within a given pixel [11]. It is important to notice that this problem is not a classical detection one, as the background power is different under the two hypotheses (background-only versus target-plus-background). Recent efforts for the development of detectors based on the replacement model can be found in [12], [13]. In [12], the analogous of Kelly's Generalized Likelihood Ratio Test (GLRT) [14] for the replacement model, namely the Adaptive Cell Under Test Estimator (ACUTE), is derived, allowing for the detection of small targets with adaptivity with respect to the background abundance estimated in the PUT. A modified version of the replacement model is developed in [13], where the GLRT is derived in the presence of a residual additive noise.

However, since in the hyperspectral sensors the spectra of different sub-pixel targets are mixed together with the background spectrum, a *generalized replacement model* is proposed in this paper, where the sum of the total amount of both multiple sub-pixel targets and background spectra is equal to one, as explained ahead. In this way, the problem of detecting the presence of multiple sub-pixel targets is formulated as a binary hypothesis test where under the alternative hypothesis the target is modeled in terms of a linear combination of endmembers whose coefficients also account for the presence of the background. This model allows us to detect and identify one or more targets from a wide spectral library of plausible targets, such as different car types in a parking area, or a single target characterized by multiple spectral signatures, such as the pickup truck not considered

in [12]. The detection problem at hand is solved by deriving decision rules where the unknown parameters, the background statistics, and the abundance vector are replaced by suitable estimates based upon available secondary data collected around the PUT. Particularly, an iterative approach is proposed for the estimation of the unknown abundance vector and two different solutions (heuristic and constrained solutions) are considered at this end. Finally, it is worth noticing that, as a byproduct, the devised detection architectures allow identifying the specific sub-pixel targets in the PUT, from the spectral library of possible endmembers, by exploiting their corresponding estimated abundances.

The remainder of the paper is organized as follows. Section II is devoted to the replacement model and the formal statement of the detection problem. Two detection architectures are derived in Section III, which differ for the estimation of the target abundances. In Section IV, the behavior of the proposed architectures is investigated by means of both simulated as well as real data. Finally, concluding remarks end this article in Section V. Some derivations are confined to the appendices.

II. PROBLEM STATEMENT

This section defines a generalization of the so called replacement model [12] that will be used to perform the detection in our case. To this end, let us consider a hyperspectral sensor able to collect the reflected light (i.e., radiance) from the observed scene through a large number, say N , of spectral bands. The radiance is generally converted into a reflectance spectrum to remove the effects of the non-uniform sun power-spectral density and the atmospheric contribution [15], [16]. The observed reflectance data samples from a given pixel can be grouped to form an N -dimensional vector, namely,

$$\mathbf{y} = [y_1, y_2, \dots, y_N]^T \in \mathbb{R}^{N \times 1}.$$

In this work, a generalization of the replacement model [16] is adopted, in which the presence of multiple sub-pixel targets (or otherwise stated endmembers) is supposed. The spectrum of each pixel can be expressed as a linear combination of r endmembers plus the background component (that is, non-target)

$$\mathbf{y} = \mathbf{T}\boldsymbol{\alpha} + (1 - \boldsymbol{\alpha}^T \mathbf{1}) \mathbf{b}, \quad (1)$$

where:

- $\mathbf{T} = [\mathbf{t}_1, \dots, \mathbf{t}_r] \in \mathbb{R}^{N \times r}$ denotes the endmember matrix (the columns are their spectral signatures);
- $\boldsymbol{\alpha} = [\alpha_1, \dots, \alpha_r]^T \in \mathbb{R}^{r \times 1}$ is the vector of the unknown fill factors subject to the constraints

$$\alpha_i \geq 0, \forall i \in \{1, \dots, r\} \text{ and } \sum_{i=1}^r \alpha_i < 1; \quad (2)$$

- $\mathbf{b} \in \mathbb{R}^{N \times 1}$ is the background spectral signature.

This model is reasonable because it is likely for a pixel to comprise one or more target materials, due to the low spatial resolution of the majority of hyperspectral sensors. The spectra of the different sub-pixel targets are mixed together (weighted by their respective abundances or fill factors) and with the spectrum of the background. As the abundances represent the proportion of the corresponding endmembers, the amount of both the sub-pixel targets and the background spectra is subject to the constraint that their sum is one. A special case of (1) is when $\alpha_i = 0, \forall i \in \{1, \dots, r\}$, which implies the absence of

targets, i.e., the presence of background only. On the contrary, due to the strict inequality in (2), the model does not admit the complete absence of the background's component. Moreover, we assume that a set of data, i.e., $\mathbf{z}_1, \dots, \mathbf{z}_K$, $K > N$, collected in the proximity of \mathbf{y} and sharing the same background properties of \mathbf{y} , is available. These data, used for estimation purposes, are assumed independent and identically distributed.

The detection problem aims at choosing between the null hypothesis \mathcal{H}_0 ($\alpha_i = 0, \forall i \in \{1, \dots, r\}$) and the alternative hypothesis \mathcal{H}_1 ($\alpha_i \neq 0$, for at least one $i \in \{1, \dots, r\}$). Using this system model, we can express our problem as the following binary hypothesis test

$$\begin{cases} \mathcal{H}_0 : \begin{cases} \mathbf{y} = \mathbf{b}, \\ \mathbf{z}_k = \mathbf{b}_k, \quad k = 1, \dots, K, \end{cases} \\ \mathcal{H}_1 : \begin{cases} \mathbf{y} = \mathbf{T}\boldsymbol{\alpha} + (1 - \boldsymbol{\alpha}^T \mathbf{1}) \mathbf{b}, \\ \mathbf{z}_k = \mathbf{b}_k, \quad k = 1, \dots, K, \end{cases} \end{cases} \quad (5)$$

with \mathbf{b} and $\mathbf{b}_k \sim \mathcal{N}_N(\boldsymbol{\mu}, \mathbf{M})$, $k = 1, \dots, K$. It is also supposed that \mathbf{b} and \mathbf{b}_k are statistically independent. Notice that the detection problem presupposes that the background power varies between the two competing hypotheses.

Before concluding this section, we provide the expressions of the joint PDF of \mathbf{y} and $\mathbf{Z} = [\mathbf{z}_1, \dots, \mathbf{z}_K]$ under \mathcal{H}_0 and \mathcal{H}_1 that are given in (3) and (4) (shown at the bottom of this page), respectively.

III. GLRT-BASED DETECTOR DESIGNS

In this section, we design decision rules for problem (5) that are based upon the GLRT. Specifically, we modify this design procedure by exploiting suitable estimates for $\boldsymbol{\alpha}$ that are different from the Maximum Likelihood Estimate (MLE). This choice is dictated by the difficult mathematics arising from the application of the maximum likelihood approach to the estimation of $\boldsymbol{\alpha}$ as required by the GLRT criterion. Therefore, we start from the general equation of the GLRT, that is

$$\frac{\max_{\boldsymbol{\mu}, \mathbf{M}, \boldsymbol{\alpha}} f_1(\mathbf{y}, \mathbf{Z}; \boldsymbol{\mu}, \mathbf{M}, \boldsymbol{\alpha})}{\max_{\boldsymbol{\mu}, \mathbf{M}} f_0(\mathbf{y}, \mathbf{Z}; \boldsymbol{\mu}, \mathbf{M})} \underset{H_0}{\overset{H_1}{>}} \eta, \quad (6)$$

where η is the detection threshold¹ set according to a given probability of false alarm (or probability of type I error), and proceed by separately solving the two optimization problems.

Under \mathcal{H}_0 , the problem at hand is well-known and, hence, for brevity, we show below the final results only. The MLEs of $\boldsymbol{\mu}$

and \mathbf{M} are given by

$$\hat{\boldsymbol{\mu}}_0 = \frac{1}{K+1}(\mathbf{y} + \tilde{\mathbf{z}}) \quad (7)$$

with $\tilde{\mathbf{z}} = \sum_{k=1}^K \mathbf{z}_k$ and

$$\widehat{\mathbf{M}}_0 = \frac{\left[(\mathbf{y} - \hat{\boldsymbol{\mu}}_0)(\mathbf{y} - \hat{\boldsymbol{\mu}}_0)^T + \sum_{k=1}^K (\mathbf{z}_k - \hat{\boldsymbol{\mu}}_0)(\mathbf{z}_k - \hat{\boldsymbol{\mu}}_0)^T \right]}{K+1}, \quad (8)$$

respectively, and the final compressed log-likelihood under \mathcal{H}_0 is²

$$L_0(\hat{\boldsymbol{\mu}}_0, \widehat{\mathbf{M}}_0) = -C_1 - C_2 \log \det(\widehat{\mathbf{M}}_0) - NC_2, \quad (9)$$

where $C_1 = [(K+1)N/2] \log(2\pi)$ and $C_2 = (K+1)/2$.

Now, we focus on the \mathcal{H}_1 hypothesis and write the corresponding log-likelihood (see (4))

$$L_1(\boldsymbol{\mu}, \mathbf{M}, \boldsymbol{\alpha}) = -C_1 - N \log A - C_2 \log(\det \mathbf{M}) - \frac{\|\mathbf{M}^{-1/2}(\mathbf{x} - A\boldsymbol{\mu})\|^2}{2A^2} - \sum_{k=1}^K \frac{\|\mathbf{M}^{-1/2}(\mathbf{z}_k - \boldsymbol{\mu})\|^2}{2}, \quad (10)$$

where $A = (1 - \boldsymbol{\alpha}^T \mathbf{1})$ and $\mathbf{x} = \mathbf{y} - \mathbf{T}\boldsymbol{\alpha}$. We first maximize $L_1(\boldsymbol{\mu}, \mathbf{M}, \boldsymbol{\alpha})$ with respect to $\boldsymbol{\mu}$, by setting to zero the corresponding derivative and obtain

$$-\frac{1}{A}\mathbf{M}^{-1}\mathbf{x} + \mathbf{M}^{-1}\boldsymbol{\mu} + \sum_{k=1}^K (-\mathbf{M}^{-1}\mathbf{z}_k + \mathbf{M}^{-1}\boldsymbol{\mu}) = 0 \quad (11)$$

$$\Rightarrow (K+1)\mathbf{M}^{-1}\boldsymbol{\mu} = \frac{1}{A}\mathbf{M}^{-1}\mathbf{x} + \mathbf{M}^{-1}\tilde{\mathbf{z}} \quad (12)$$

$$\Rightarrow \hat{\boldsymbol{\mu}} = \frac{1}{K+1} \left(\frac{1}{A}\mathbf{x} + \tilde{\mathbf{z}} \right). \quad (13)$$

Using the above result in (10), after some algebraic manipulations, the partially-compressed log-likelihood can be recast as

$$L_1(\hat{\boldsymbol{\mu}}, \mathbf{M}, \boldsymbol{\alpha}) = -C_1 - N \log A - C_2 \log(\det \mathbf{M}) - \text{Tr} \left\{ \frac{\mathbf{M}^{-1}}{2} \left[\left(\frac{1}{A}\mathbf{x} - \hat{\boldsymbol{\mu}} \right) \left(\frac{1}{A}\mathbf{x} - \hat{\boldsymbol{\mu}} \right)^T + \sum_{k=1}^K (\mathbf{z}_k - \hat{\boldsymbol{\mu}})(\mathbf{z}_k - \hat{\boldsymbol{\mu}})^T \right] \right\}. \quad (14)$$

¹Hereafter, we use symbol η to denote the generic threshold.

²For simplicity, in what follows, we omit the dependence of the log-likelihood function on data \mathbf{y} and \mathbf{Z} .

$$f_0(\mathbf{y}, \mathbf{Z}; \boldsymbol{\mu}, \mathbf{M}) = \left(\frac{1}{(2\pi)^{N/2} \det(\mathbf{M})^{1/2}} \right)^{K+1} \exp \left\{ -\frac{1}{2} \text{Tr} \left[\mathbf{M}^{-1} \left((\mathbf{y} - \boldsymbol{\mu})(\mathbf{y} - \boldsymbol{\mu})^T + \sum_{k=1}^K (\mathbf{z}_k - \boldsymbol{\mu})(\mathbf{z}_k - \boldsymbol{\mu})^T \right) \right] \right\}. \quad (3)$$

$$f_1(\mathbf{y}, \mathbf{Z}; \boldsymbol{\mu}, \mathbf{M}, \boldsymbol{\alpha}) = \left(\frac{1}{(2\pi)^{N/2} (1 - \boldsymbol{\alpha}^T \mathbf{1})^{N/(K+1)} \det(\mathbf{M})^{1/2}} \right)^{K+1} \times \exp \left\{ -\frac{1}{2} \text{Tr} \left[\mathbf{M}^{-1} \left(\frac{(\mathbf{y} - \mathbf{T}\boldsymbol{\alpha} - (1 - \boldsymbol{\alpha}^T \mathbf{1})\boldsymbol{\mu})(\mathbf{y} - \mathbf{T}\boldsymbol{\alpha} - (1 - \boldsymbol{\alpha}^T \mathbf{1})\boldsymbol{\mu})^T}{(1 - \boldsymbol{\alpha}^T \mathbf{1})^2} + \sum_{k=1}^K (\mathbf{z}_k - \boldsymbol{\mu})(\mathbf{z}_k - \boldsymbol{\mu})^T \right) \right] \right\}. \quad (4)$$

The MLE of \mathbf{M} under \mathcal{H}_1 can be computed by resorting to the following inequality [17] $\log \det(\mathbf{A}) \leq \text{Tr}[\mathbf{A}] - N$, where \mathbf{A} is any N -dimensional matrix with nonnegative eigenvalues, and, hence, we come up with

$$\widehat{\mathbf{M}} = \frac{\left[\left(\frac{1}{A} \mathbf{x} - \widehat{\boldsymbol{\mu}} \right) \left(\frac{1}{A} \mathbf{x} - \widehat{\boldsymbol{\mu}} \right)^T + \sum_{k=1}^K (\mathbf{z}_k - \widehat{\boldsymbol{\mu}}) (\mathbf{z}_k - \widehat{\boldsymbol{\mu}})^T \right]}{K+1}. \quad (15)$$

Hence, we update (14) with $\widehat{\mathbf{M}}$ and find

$$L_1(\widehat{\boldsymbol{\mu}}, \widehat{\mathbf{M}}, \boldsymbol{\alpha}) = -C_3 - N \log A - C_2 \log \det \left[\left(\frac{1}{A} \mathbf{x} - \widehat{\boldsymbol{\mu}} \right) \times \left(\frac{1}{A} \mathbf{x} - \widehat{\boldsymbol{\mu}} \right)^T + \sum_{k=1}^K (\mathbf{z}_k - \widehat{\boldsymbol{\mu}}) (\mathbf{z}_k - \widehat{\boldsymbol{\mu}})^T \right], \quad (16)$$

where $C_3 = C_1 + \frac{1}{2}(K+1)N - C_2N \log(K+1)$. In Appendix A, we show that the argument of the determinant in (16) can be suitably manipulated leading to the following expression for the partially-compressed log-likelihood function

$$\begin{aligned} L_1(\widehat{\boldsymbol{\mu}}, \widehat{\mathbf{M}}, \boldsymbol{\alpha}) &= -C_3 - N \log A - C_2 \log(\det \mathbf{S}_1) - C_2 \\ &\times \log \left(1 + \frac{K}{K+1} \left(\frac{1}{A} \mathbf{x} - \frac{1}{K} \tilde{\mathbf{z}} \right)^T \mathbf{S}_1^{-1} \left(\frac{1}{A} \mathbf{x} - \frac{1}{K} \tilde{\mathbf{z}} \right) \right) \\ &= -C_3 - N \log(1 - \boldsymbol{\alpha}^T \mathbf{1}) - C_2 \log(\det \mathbf{S}_1) \\ &- C_2 \log \left(1 + C_4 \left\| \mathbf{S}_1^{-1/2} \left(\frac{\mathbf{y} - \mathbf{T}\boldsymbol{\alpha}}{1 - \boldsymbol{\alpha}^T \mathbf{1}} - \tilde{\mathbf{z}} \right) \right\|^2 \right), \quad (17) \end{aligned}$$

where $\mathbf{S}_1 = \mathbf{S} - \frac{1}{K(K+1)} \tilde{\mathbf{z}} \tilde{\mathbf{z}}^T$ with $\mathbf{S} = \mathbf{Z}\mathbf{Z}^T - \frac{1}{K+1} \tilde{\mathbf{z}} \tilde{\mathbf{z}}^T$, $C_4 = \frac{K}{K+1}$, and $\tilde{\mathbf{z}} = \frac{1}{K} \tilde{\mathbf{z}}$. Since we are interested in the maximization of the partially-compressed log-likelihood with respect to $\boldsymbol{\alpha}$, we focus on the terms that depend on $\boldsymbol{\alpha}$ only and define the following function

$$\begin{aligned} g(\boldsymbol{\alpha}) &= N \log(1 - \boldsymbol{\alpha}^T \mathbf{1}) \\ &+ C_2 \log \left[1 + \left\| \left(\frac{\mathbf{y}_0 - \mathbf{T}_0 \boldsymbol{\alpha}}{1 - \boldsymbol{\alpha}^T \mathbf{1}} - \tilde{\mathbf{z}}_0 \right)^T \right\|^2 \right] \quad (18) \end{aligned}$$

where $\mathbf{y}_0 = C_4^{1/2} \mathbf{S}_1^{-1/2} \mathbf{y}$, $\mathbf{T}_0 = C_4^{1/2} \mathbf{S}_1^{-1/2} \mathbf{T}$ and $\tilde{\mathbf{z}}_0 = C_4^{1/2} \mathbf{S}_1^{-1/2} \tilde{\mathbf{z}}$. The maximization of (17) with respect to $\boldsymbol{\alpha}$ is equivalent to the problem

$$\begin{cases} \min_{\boldsymbol{\alpha}} & g(\boldsymbol{\alpha}) \\ \text{subject to} & \sum_{i=1}^r \alpha_i < 1, \\ & \alpha_i \geq 0, \quad \forall i \in \{1, \dots, r\}. \end{cases} \quad (19)$$

In the next subsection, we describe two different procedures to solve problem (19). Denoting by $\widehat{\boldsymbol{\alpha}}$ the generic solution returned by these procedures, we use it in (17) and the final expression of the detection architecture is

$$L_1(\widehat{\boldsymbol{\mu}}, \widehat{\mathbf{M}}, \widehat{\boldsymbol{\alpha}}) \underset{H_0}{\overset{H_1}{>}} L_0(\widehat{\boldsymbol{\mu}}_0, \widehat{\mathbf{M}}_0) \underset{H_0}{>} \eta. \quad (20)$$

A. Solution to (19)

The approach devised here relies on an iterative solution of (19). In particular, we firstly highlight the dependence of the objective function from a single entry of $\boldsymbol{\alpha}$, say α_j , and then, at each iteration, we minimize $g(\boldsymbol{\alpha})$ with respect to α_j as the index j varies. To this end, let us notice that

$$1 - \boldsymbol{\alpha}^T \mathbf{1} = 1 - \sum_{i=1}^r \alpha_i = 1 - \sum_{i \neq j} \alpha_i - \alpha_j = a_j - \alpha_j \quad (21)$$

where $a_j = 1 - \sum_{i \neq j} \alpha_i$ with $0 < a_j < 1$. Moreover, we have that

$$\begin{aligned} \mathbf{y}_0 - \mathbf{T}_0 \boldsymbol{\alpha} &= \mathbf{y}_0 - [\mathbf{t}_{01}, \dots, \mathbf{t}_{0N}] \boldsymbol{\alpha} \\ &= \mathbf{y}_0 - \sum_{i \neq j} \mathbf{t}_{0i} \alpha_i - \mathbf{t}_{0j} \alpha_j = \mathbf{y}_j - \mathbf{t}_{0j} \alpha_j \quad (22) \end{aligned}$$

with $\mathbf{y}_j = \mathbf{y}_0 - \sum_{i \neq j} \mathbf{t}_{0i} \alpha_i$. The estimation procedure iterates according to the following rationale. Denoting by t the iteration index and given the estimates $\alpha_i^{(t+1)}$ (at the $(t+1)$ th iteration), $i = 1, \dots, j-1$, and $\alpha_i^{(t)}$ (at the t th iteration), $i = j+1, \dots, r$, we exploit $g(\boldsymbol{\alpha})$ to build up the following function of α_j

$$\begin{aligned} g(\alpha_j) &= N \log \left(\widehat{a}_j^{(t,t+1)} - \alpha_j \right) + C_2 \\ &\times \log \left[1 + \left\| \left(\frac{\widehat{\mathbf{y}}_j^{(t,t+1)} - \mathbf{t}_{0j} \alpha_j}{\widehat{a}_j^{(t,t+1)} - \alpha_j} - \tilde{\mathbf{z}}_0 \right) \right\|^2 \right], \quad (23) \end{aligned}$$

where $\widehat{a}_j^{(t,t+1)} = 1 - \sum_{i=1}^{j-1} \alpha_i^{(t+1)} - \sum_{i=j+1}^r \alpha_i^{(t)}$ and $\widehat{\mathbf{y}}_j^{(t,t+1)} = \mathbf{y}_0 - \sum_{i=1}^{j-1} \mathbf{t}_{0i} \alpha_i^{(t+1)} - \sum_{i=j+1}^r \mathbf{t}_{0i} \alpha_i^{(t)}$. This function is then used to come up with the update of the estimate of α_j at the $(t+1)$ th iteration. Specifically, in the next subsections, we devise two different approaches: the first is heuristic whereas the second incorporates the constrained solutions of (19) at the design stage. An initial estimate of α_i , $i = 1, \dots, r$ is necessary to initialize the algorithms as well as a reasonable stopping criterion as, for instance, setting a maximum number of iterations, say N_{iter} .

1) *Heuristic Solution:* Let us recast (23) as

$$\begin{aligned} g(\alpha_j) &= N \log \left(\widehat{a}_j^{(t,t+1)} - \alpha_j \right) + C_2 \\ &\times \left[\log(D_0 + D_1 \alpha_j + D_2 \alpha_j^2) \right. \\ &\left. - 2 \log \left(\widehat{a}_j^{(t,t+1)} - \alpha_j \right) \right], \quad (24) \end{aligned}$$

where $D_0 = (\widehat{\mathbf{y}}_j^{(t,t+1)})^T \widehat{\mathbf{y}}_j^{(t,t+1)} - 2\widehat{a}_j^{(t,t+1)} (\widehat{\mathbf{y}}_j^{(t,t+1)})^T \tilde{\mathbf{z}}_0 + (\widehat{a}_j^{(t,t+1)})^2 \tilde{\mathbf{z}}_0^T \tilde{\mathbf{z}}_0 + (\widehat{a}_j^{(t,t+1)})^2$; $D_1 = 2[\widehat{a}_j^{(t,t+1)} (\mathbf{t}_{0j}^T \tilde{\mathbf{z}}_0 - \tilde{\mathbf{z}}_0^T \tilde{\mathbf{z}}_0) + (\widehat{\mathbf{y}}_j^{(t,t+1)})^T \tilde{\mathbf{z}}_0 - (\widehat{\mathbf{y}}_j^{(t,t+1)})^T \mathbf{t}_{0j}] - 2\widehat{a}_j^{(t,t+1)}$; and $D_2 = 1 + \mathbf{t}_{0j}^T \mathbf{t}_{0j} - 2\mathbf{t}_{0j}^T \tilde{\mathbf{z}}_0 + \tilde{\mathbf{z}}_0^T \tilde{\mathbf{z}}_0$.

Setting to zero the first derivative of (24) with respect to α_j leads to the following quadratic equation

$$\begin{aligned} -ND_2 \alpha_j^2 + [2C_2 D_2 \widehat{a}_j^{(t,t+1)} + (C_2 - N) D_1] \alpha_j \\ + [C_2 D_1 \widehat{a}_j^{(t,t+1)} + 2D_0 C_2 - ND_0] = 0. \quad (25) \end{aligned}$$

Now, we can evaluate $\widehat{\alpha}_j^{(t+1)}$ by choosing the real-valued positive solution of (25) returning the minimum value of (24).

However, since the constraint (2) must be satisfied, we regularize $\tilde{\alpha}_i^{(t+1)}$, $i = 1, \dots, r$, as follows

$$\hat{\alpha}_i^{(t+1)} = \tilde{\alpha}_i^{(t+1)} \frac{(1 - \alpha_b)}{\sum_{i=1}^r \tilde{\alpha}_i^{(t+1)}}, \quad (26)$$

where $0 \leq \alpha_b < 1$ represents the unknown background abundance; in practice, it can be set using a linear grid of values (sized according to the available a priori information) and selecting the value that minimizes the objective function. This heuristic algorithm is summarized in Algorithm 1.

Algorithm 1: Estimation Procedure for α_j (heuristic solution).

Input: $\mathbf{T}_0, \mathbf{y}_0, \tilde{\mathbf{z}}_0, \alpha_i^{(0)}, i = 1, \dots, r, N_{iter}$

Output: $\hat{\alpha}$

- 1: Set $t = 1$
- 2: Set $j = 1$
- 3: Compute $\hat{a}_j^{(t-1,t)} = 1 - \sum_{i=1}^{j-1} \alpha_i^{(t)} - \sum_{i=j+1}^r \alpha_i^{(t-1)}$
- 4: Select the j th column of \mathbf{T}_0 , i.e., \mathbf{t}_{0j}
- 5: Compute $\mathbf{y}_j^{(t-1,t)} = \mathbf{y}_0 - \sum_{i=1}^{j-1} \mathbf{t}_{0i} \alpha_i^{(t)} - \sum_{i=j+1}^r \mathbf{t}_{0i} \alpha_i^{(t-1)}$
- 6: Compute $\tilde{\alpha}_j^{(t)}$ by solving (25) and selecting the positive real-valued solution that minimizes (24)
- 7: If $j < r$, set $j = j + 1$ and go to step 3 else go to step 8
- 8: Normalize $\tilde{\alpha}^{(t)} = [\tilde{\alpha}_1^{(t)}, \dots, \tilde{\alpha}_r^{(t)}]^T$ as in (26) to obtain $\hat{\alpha}^{(t)} = [\hat{\alpha}_1^{(t)}, \dots, \hat{\alpha}_r^{(t)}]^T$
- 9: If $t < N_{iter}$, set $t = t + 1$ and go to step 2 else go to step 10
- 10: Return $\hat{\alpha} = [\hat{\alpha}_1^{(t)}, \dots, \hat{\alpha}_r^{(t)}]^T$

2) *Constrained Solutions:* Let us introduce an auxiliary variable, say β_j , such that

$$\beta_j + \sum_{i=1}^{j-1} \alpha_i^{(t+1)} + \sum_{i=j+1}^r \alpha_i^{(t)} + \alpha_j = 1 \quad (27)$$

$$\Rightarrow \beta_j + \alpha_j = \hat{a}_j^{(t,t+1)}. \quad (28)$$

Then, we exploit β_j to modify (23) by incorporating the model constraint on the abundances, namely

$$g(\alpha_j, \beta_j) = N \log \beta_j + C_2 \times \log \left[1 + \left\| \left(\frac{\hat{\mathbf{y}}_j^{(t,t+1)} - \mathbf{t}_{0j} \alpha_j}{\beta_j} - \tilde{\mathbf{z}}_0 \right) \right\|^2 \right], \quad (29)$$

and consider the following minimization problem

$$\begin{cases} \min_{\alpha_j, \beta_j} g(\alpha_j, \beta_j) \\ \text{subject to } \alpha_j + \beta_j = \hat{a}_j^{(t,t+1)} \end{cases} \quad (30)$$

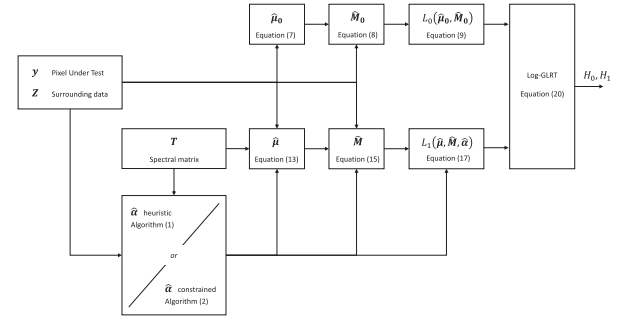


Fig. 1. Signal processing chain leading to the proposed detectors.

Now, we apply the method of Lagrange multipliers and define the Lagrangian

$$\mathcal{L}(\alpha_j, \beta_j) = g(\alpha_j, \beta_j) - \lambda (\alpha_j + \beta_j - \hat{a}_j^{(t,t+1)}), \quad (31)$$

where λ is a Lagrange multiplier. Setting to zero the gradient of the Lagrangian and considering the constraint equation, we form the following system of equations

$$\begin{cases} \lambda A_1 \alpha_j^2 + (\lambda A_2 - 2C_2 A_1) \alpha_j + \lambda A_3 - C_2 A_2 = 0 \\ -\lambda B_1 \beta_j^3 + (N B_1 - \lambda B_2) \beta_j^2 + (N B_2 - C_2 B_2 - \lambda B_3) \beta_j \\ + N B_3 - 2C_2 B_3 = 0 \\ \alpha_j + \beta_j = \hat{a}_j^{(t,t+1)} \end{cases} \quad (32)$$

where $A_1 = \mathbf{t}_{0j}^T \mathbf{t}_{0j}$; $A_2 = 2[\beta_j \mathbf{t}_{0j}^T \tilde{\mathbf{z}}_0 - (\hat{\mathbf{y}}_j^{(t,t+1)})^T \mathbf{t}_{0j}]$; $A_3 = \beta_j^2 (1 + \tilde{\mathbf{z}}_0^T \tilde{\mathbf{z}}_0) - 2\beta_j (\hat{\mathbf{y}}_j^{(t,t+1)})^T \tilde{\mathbf{z}}_0 + (\hat{\mathbf{y}}_j^{(t,t+1)})^T \hat{\mathbf{y}}_j^{(t,t+1)}$; $B_1 = (1 + \tilde{\mathbf{z}}_0^T \tilde{\mathbf{z}}_0)$; $B_2 = 2[\alpha_j \mathbf{t}_{0j}^T \tilde{\mathbf{z}}_0 - (\hat{\mathbf{y}}_j^{(t,t+1)})^T \tilde{\mathbf{z}}_0]$; $B_3 = (\hat{\mathbf{y}}_j^{(t,t+1)})^T \hat{\mathbf{y}}_j^{(t,t+1)} - 2\alpha_j (\hat{\mathbf{y}}_j^{(t,t+1)})^T \mathbf{t}_{0j} + \alpha_j^2 \mathbf{t}_{0j}^T \mathbf{t}_{0j}$.

Finally, the estimate of $\hat{\alpha}_j$, say $\hat{a}_j^{(t,t+1)}$, is obtained by selecting the real-valued positive solution that is strictly lower than 1 and minimizes the objective function as summarized in Algorithm 2. A block diagram of the signal processing chain towards the formation of the detectors is shown in Fig. 1.

Before investigating the performance of both solutions, it is important to notice that the convergence to the global minimum is not guaranteed. Nevertheless, it can be shown that $g(\alpha)$ is limited from below (provided that $K > N$) and the constrained solution gives rise to a nonincreasing sequence of values for $g(\alpha)$ satisfying the constraint (19). It follows that the constrained algorithm converges at least to a local constrained stationary point. On the other hand, the heuristic approach, which is less time demanding than the constrained algorithm, due to the normalization (26), is not guaranteed to return a nonincreasing sequence of the objective function as highlighted by the numerical examples of the next section, where it is shown that the convergence curves experience a plateau as the number of iterations grows.

IV. PERFORMANCE ANALYSIS

In this section, we assess the detection performance of the proposed detectors through numerical examples based on simulated as well as real data. To this end, we resort to a hyperspectral

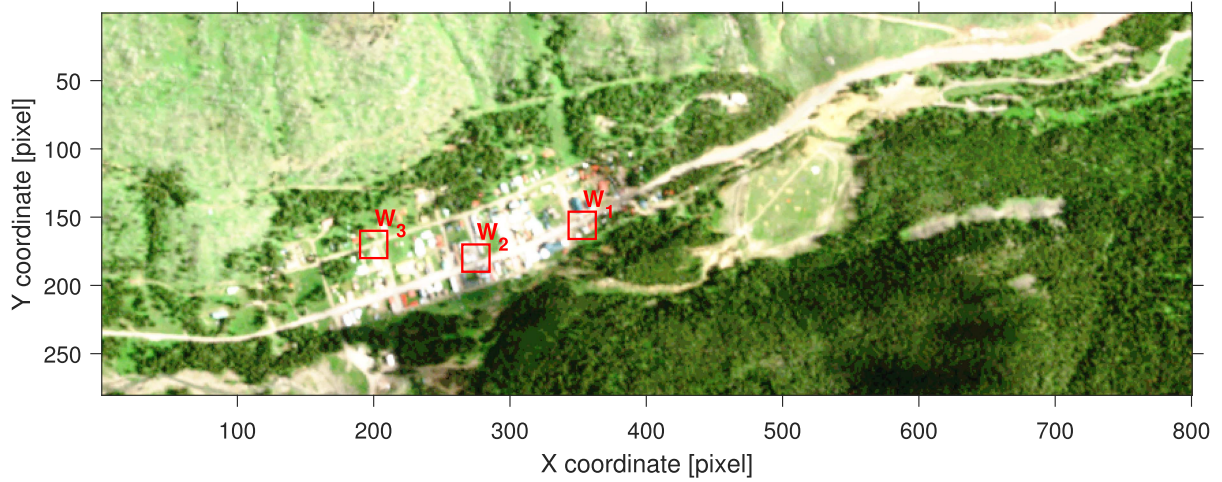


Fig. 2. Cooke City scene of the RIT dataset in RGB representation combining bands 15, 8, and 3 respectively. W_1 , W_2 and W_3 represent the three test windows used to perform the multiple sub-pixel target analysis described in the following sections.

Algorithm 2: Estimation Procedure for α_j (constrained solution).

Input: $\mathbf{T}_0, \mathbf{y}_0, \tilde{\mathbf{z}}_0, \alpha_i^{(0)}, i = 1, \dots, r, N_{iter}$

Output: $\hat{\alpha}$

1: Set $t = 1$

2: Set $j = 1$

3: Compute $\hat{\alpha}_j^{(t-1,t)} = 1 - \sum_{i=1}^{j-1} \alpha_i^{(t)} - \sum_{i=j+1}^r \alpha_i^{(t-1)}$

4: Select the j th column of \mathbf{T}_0 , i.e., \mathbf{t}_{0j}

5: Compute $\mathbf{y}_j^{(t-1,t)} = \mathbf{y}_0 - \sum_{i=1}^{j-1} \mathbf{t}_{0i} \alpha_i^{(t)}$

$$- \sum_{i=j+1}^r \mathbf{t}_{0i} \alpha_i^{(t-1)}$$

6: Compute $\hat{\alpha}_j^{(t)}$ by solving (32) and selecting the real-valued positive solution that is strictly lower than 1 and minimizes (29)

7: If $j < r$, set $j = j + 1$ and go to step 3 else go to step 8

8: If $t < N_{iter}$ set $t = t + 1$ and go to step 2 else go to step 9

9: Return $\hat{\alpha} = [\hat{\alpha}_1^{(t)}, \dots, \hat{\alpha}_r^{(t)}]^T$

dataset, namely the Rochester Institute of Technology (RIT) experiment³ [18]. The RIT open data experiment has been specially designed for target detection and has been widely used in the open literature [12], [19]. Indeed, a corrected and geo-registered reflectance map is available so that the detection performance will be independent from any particular experimental setup.

Data were collected in July 2006 with a coverage area of approximately 2.0 km² and around the small town of Cooke City, Montana, USA. To this end, the airborne HyMap sensor operated by HyVista was used [20]. The images were acquired flying at 1.4 km above the ground and were successively geo-registered using ground control points. Both calibrated spectral radiance

as well as spectral reflectance after atmospheric compensation are available in the dataset.

The Cooke City scene is shown in Fig. 2, which is composed of 280 × 800 pixels. Each pixel is observed at 126 spectral bands covering the electromagnetic spectrum from 0.45 μm to 2.48 μm with a ground resolution of about 3.0 × 3.0 m. It is important to note that the spatial resolution of the map is of the same order of magnitude as the target sizes, so that they will usually behave as sub-pixel targets [21], [22].

In this dataset, civilian vehicles and small fabric panels were used as targets. Specifically, three kinds of cars (indicated as V_1 , V_2 and V_3) and four different fabric panels (F_1 , F_2 , F_3 and F_4) are present in the scene. It is important to highlight that V_2 is a pick-up characterized by two different spectral signatures, namely, one corresponding to the cabin (V_{2c}) and the other to the back (V_{2b}), so it can be considered as an example of multi-target. For each target, a reference spectrum signature obtained from a laboratory spectrophotometer is provided together with the RIT dataset, as shown in Fig. 3.

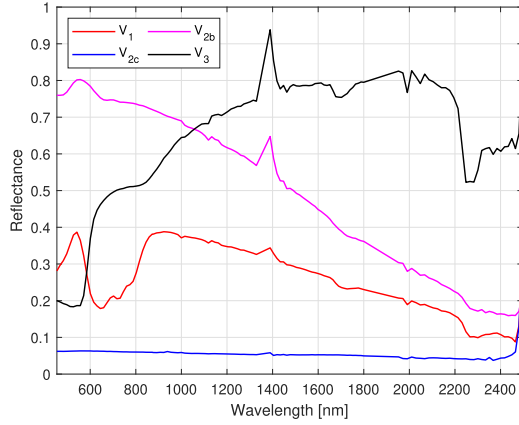
Finally, the RIT dataset provides a standard self-test where the targets' map positions are known, and also a blind test with unknown target positions to prevent ad hoc algorithms. Moreover, the water absorption and low signal-to-noise bands were identified and removed from the Cooke City dataset for further processing. Precisely, bands no. 1, 2, 3, 63, 64, 65, 66, 95, 96, and 97 were discarded as in [23]. After removing these bands, 116 spectral bands were retained.

A. Results on Simulated Data

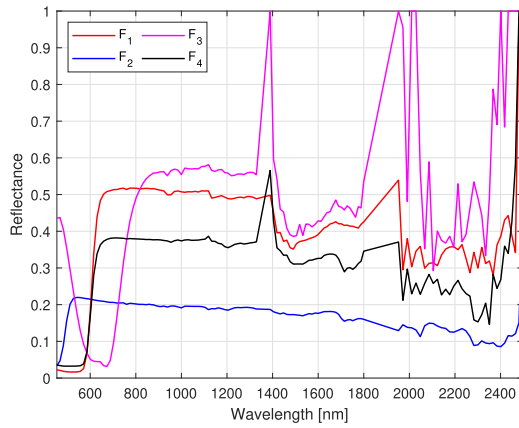
In this subsection, a reflectance pixel containing the target vehicle V_2 is simulated according to the replacement model defined in (1). Particularly, the considered endmembers' matrix is composed of three spectral signatures

$$\mathbf{T} = [\mathbf{t}_{2c}, \mathbf{t}_{2b}, \mathbf{t}_3] \in \mathbb{R}^{116 \times 3},$$

³Data can be downloaded from [Online]. Available: <http://dirsapps.cis.rit.edu>



(a) Vehicles spectral signatures



(b) Fabric panels spectral signatures

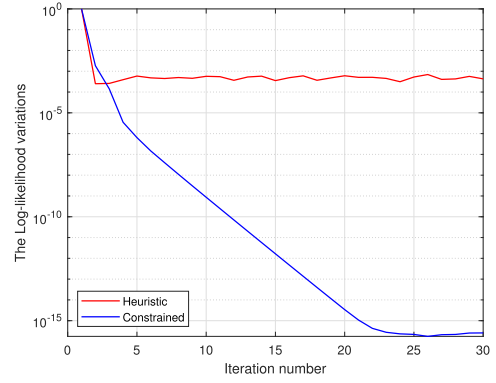
Fig. 3. Targets spectral signatures of RIT dataset.

TABLE I
ABUNDANCES FOR DIFFERENT SIMULATED PIXEL TEST CASES.
 α_{2c} , α_{2b} , AND α_3 ARE THE ABUNDANCES REFERRED TO
THE ENDMEMBERS V_{2c} , V_{2b} , AND V_3 , RESPECTIVELY

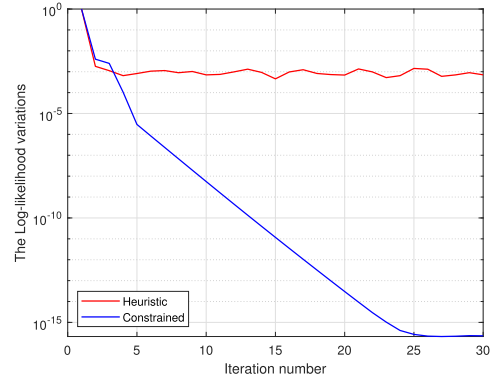
$(\alpha_{2c}, \alpha_{2b}, \alpha_3)$	abundances' sum	background's abundance
(0.00, 0.00, 0)	0.00	1.00
(0.31, 0.01, 0)	0.32	0.68
(0.32, 0.02, 0)	0.34	0.66
(0.33, 0.03, 0)	0.36	0.64
(0.34, 0.04, 0)	0.38	0.62
(0.35, 0.05, 0)	0.40	0.60
(0.40, 0.10, 0)	0.50	0.50
(0.45, 0.15, 0)	0.60	0.40
(0.50, 0.20, 0)	0.70	0.30
(0.55, 0.25, 0)	0.80	0.20
(0.60, 0.30, 0)	0.90	0.10

where \mathbf{t}_{2c} , \mathbf{t}_{2b} , and \mathbf{t}_3 denote the spectral signatures of V_{2c} , V_{2b} , and V_3 , respectively, that are given together with the RIT dataset.

We consider different configurations for the fill factor vector of the abundances, as specified in Table I. It is important to note that for the V_{2c} endmember we assign a bigger value of abundance as its reflectance signature is lower if compared with



(a) Sum of abundances equal to 0.7



(b) Sum of abundances equal to 0.9

Fig. 4. Log-likelihood mean variation versus the iteration number over 100 MC independent trials.

V_{2b} , see Fig. 3(a). We add a background noise modeled in terms of a zero-mean Gaussian random vector with variance 0.5 and independent entries. The number of secondary data K is set to 625.

Remember that the heuristic approach, as specified in (26), requires a selection of a linear grid of values for the background abundance to minimize the objective function. Thus, we set a linear grid of values from 0.1 to 0.9, with a step of 0.01. This condition is applied for performances evaluated on both simulated and real data.

As a preliminary step, we analyze the behavior of the proposed procedures in terms of the number of iterations required for convergence. To this end, we define the Log-likelihood variation $\Delta L_1^{(h)}$ as a function of the iteration index, say h , as

$$\Delta L_1^{(h)} = \left| \frac{L_1^{(h)}(\hat{\boldsymbol{\mu}}, \widehat{\mathbf{M}}, \hat{\boldsymbol{\alpha}}) - L_1^{(h-1)}(\hat{\boldsymbol{\mu}}, \widehat{\mathbf{M}}, \hat{\boldsymbol{\alpha}})}{L_1^{(h)}(\hat{\boldsymbol{\mu}}, \widehat{\mathbf{M}}, \hat{\boldsymbol{\alpha}})} \right|. \quad (33)$$

In this analysis, two different cases are considered with abundances' sums of 0.7 and 0.9 (as in Table I), respectively. In Fig. 4, we plot the average values of (33) evaluated over 100 Monte Carlo (MC) independent trials for both the heuristic and the constrained approaches. From Fig. 4, it is clear that for the heuristic algorithm the Log-likelihood variation settles at an approximately constant value. In fact, after approximately 4 iterations, $\Delta L_1^{(h)}$ varies around 10^{-3} . Contrarily, the constrained method requires more than 20 iterations to reaches a constant value below 10^{-15} for $\Delta L_1^{(h)}$. Interestingly, both algorithms

TABLE II
EXECUTION TIMES FOR THE HEURISTIC AND CONSTRAINED APPROACHES

	Heuristic Solution	Constrained Solution
4 iterations	0.017 s	3.965 s
15 iterations	0.065 s	16.102 s

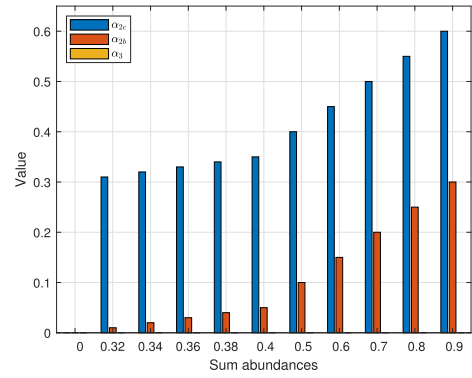
share the same behavior in terms of convergence at the initial iteration values. For further details about the convergence of these algorithms, the reader is referred to the end of Section IV, where merits and drawbacks of the proposed solutions are discussed. In the following, we will set the maximum number of iterations as $N_{iter} = 15$ which is sufficient to obtain $\Delta L_1^{(h)} < 10^{-2}$ for⁴ both heuristic and constrained approaches. Finally, in Table II, we show the execution times for a number of iterations leading to approximately the same log-likelihood variation (around 10^{-3}), namely 4 iterations, and for $N_{iter} = 15$. These values have been obtained by using an Intel(R) Core(TM) i7-7500 U coupled with Windows 10 (64 bits) and MATLAB R2019b. As expected, the heuristic approach is less time-demanding than the constrained solution but its approaching to a local stationary point is slower than the constrained algorithm.

In Fig. 5(a) we plot the true abundance's configurations specified in Table I while in Fig. 5(b) and (c) we plot the Root Mean Square (RMS) value of the estimated abundances, averaged over 1000 MC trials, for both the heuristic and the constrained approaches, respectively. It is immediately evident that the estimate trends of the heuristic and the constrained methods are very similar. Both methods, in fact, for low concentrations of targets' abundances, i.e., high background concentration, provide estimate values that differ considerably from the true ones. This behavior can be explained if we look at the Table I, where when abundance sum is less than 0.50, the single endmembers' abundances, i.e., α_{2c} , α_{2b} , and α_3 , are less than the background concentration and represent a very challenge situation. On the contrary, we notice that for abundances' sum greater than 0.50, we come up with reasonable estimates of each target's abundance. Specifically, when abundances' sum is greater than or equal to 0.80, the estimated values are very close to the true values. In these configurations, the background's concentration is less than each abundances' value.

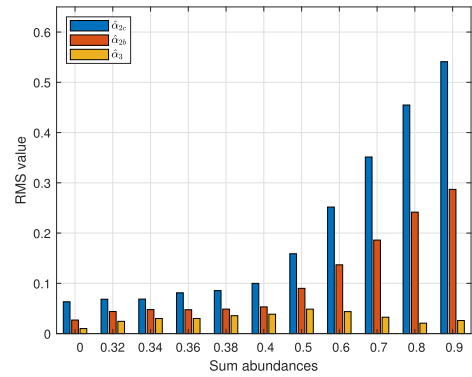
A more accurate analysis of the abundances' estimates obtained for both constrained and heuristic algorithms is performed in terms of RMS Error (RMSE), which is shown in Fig. 6. As reasonable to expect, the RMSE trend is the same for both algorithms. Specifically, from 0.32 to 0.50 of the sum of the abundances, the RMSE is almost constant and it presents the higher values. In this interval we note that the RMSE of heuristic approach is slightly less than that of the constrained one. For abundances' sum of 0.5, the RMSE begins to decrease linearly, confirming that estimated values are closer to the true ones. In this case the constrained approach provides better estimation performance than the heuristic method.

Fig. 7 shows the detection probability P_d evaluated using a false alarm probability $P_{fa} = 10^{-3}$ and 1000 MC trials. From this figure, it turns out that the P_d values of the heuristic approach are higher than those of the constrained approach in the interval of abundances less than or equal to 0.5. This trend, in

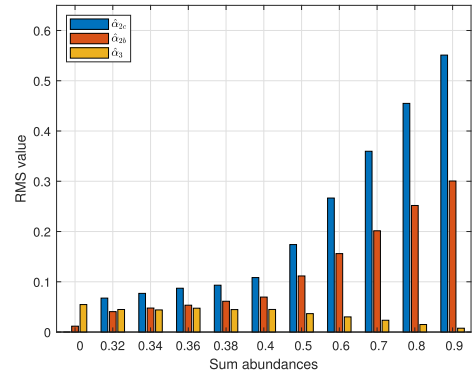
⁴Notice that 10^{-3} is approximately the plateau level for the heuristic algorithm mentioned before.



(a) True abundances as shown in Table II



(b) Estimated abundances Heuristic method



(c) Estimated abundances Constrained method

Fig. 5. RMS value of estimated abundances for the heuristic and constrained approaches over 1000 MC trials and for different background intervals.

accordance with what has already been said for the RMSE, can be due to better estimated values. For abundances' sum greater than 0.5, the detection probabilities are greater than 0.9 for both approaches. Particularly, we get closer to the maximum value for the detection probability at 0.6 and 0.7 of abundances' sum for the constrained and the heuristic approaches, respectively.

B. Results on Real Data

In this section, the performance of the proposed architectures is assessed through the real RIT dataset. This analysis allows us to quantify the robustness of the proposed detectors in the

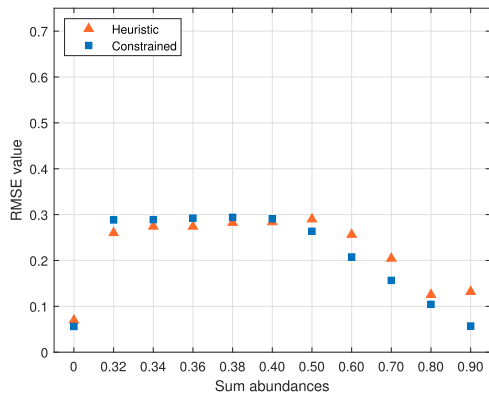


Fig. 6. RMSE value for heuristic and constrained approach computer for 1000 MC trials.

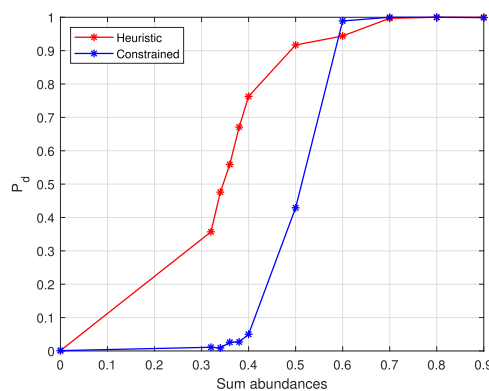


Fig. 7. Detection probability computed for $P_{fa} = 10^{-3}$ and for 1000 MC independent trials.

presence of model mismatches due to the fact that real data do not exactly match the design assumptions.

At first, we assess the performance in the case of a single sub-pixel target. To this aim, we consider a single signature and use Kelly's GLRT [14], the Adaptive Matched Filter (AMF) [24], the Adaptive Coherence Estimator (ACE) [25], [26], and the ACUTE detector, recently proposed in [12], as competitors. Next, the detection performance for multiple sub-pixel targets is analyzed.

It is important to highlight that no specific pre-processing has been applied to the real RIT dataset. Finally, for numerical reasons, we scale the reflectance spectral signature (shown in Fig. 3) by a factor of 100.

1) *Single Sub-Pixel Target Detection*: The objective of this subsection is to compare the performance of the heuristic and constrained detectors with the ACUTE detector [12]. To this end, we use the entire RIT dataset and as target of interest we consider V_3 only. The choice of the target V_3 is dictated by the fact that it is the most challenging in terms of false alarms, as shown in [12]. The V_3 target, as indicated by the information related to the dataset, has pixel coordinates: $P_3 \equiv (282, 186)$. Fig. 8 shows the spectral reflectance for this target pixel.

In order to make a comparable performance analysis with the ACUTE detector, the spectral matrix is composed of only the spectral signature of target V_3 : $\mathbf{T} \equiv \mathbf{t}_3 \in \mathbb{R}^{116 \times 1}$.

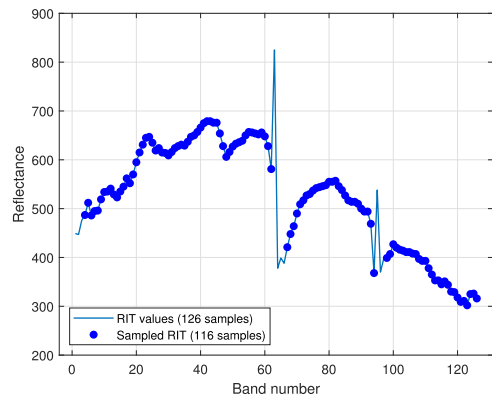


Fig. 8. Spectral reflectance of target V_3 located at pixel $P_3 \equiv (282, 186)$. Blue dots indicate the considered spectral samples to avoid water absorption and low SNR bands.

TABLE III
ABUNDANCE ESTIMATES OF TARGET V_3 AT PIXEL $P_3 \equiv (282, 186)$, FOR DIFFERENT BACKGROUND WINDOW SIZE

K	AMF	ACUTE	Heuristic	Constrained
15×15	0.141	0.003	0.100	0.051
25×25	0.270	0.039	0.100	0.051
55×55	0.243	0.142	0.140	0.136

TABLE IV
PERFORMANCE COMPARISON BETWEEN ACUTE, KELLY'S GLRT, AMF, ACE, AND THE PROPOSED DETECTORS FOR A 55×55 WINDOW SIZE IN TERMS OF FALSE ALARM RATE AND FOR TARGET V_3 OF RIT DATASET

Detector	False Alarm Percentage
Kelly's GLRT	15.977%
AMF	16.272%
ACE	10.514%
ACUTE	6.728%
Heuristic	4.453%
Constrained	4.483%

In Table III, we report the abundance's estimates relative to the target V_3 for all the considered algorithms.⁵ These results are obtained by applying three background window sizes, namely, 15×15 , 25×25 , and 55×55 pixels around the PUT; moreover, given the PUT, data for the background estimation are selected excluding the pixels belonging to a 3×3 window centered on the PUT that might contain target signatures. We note that a small background window size, such as 15×15 or 25×25 , results in low abundance's estimates of the target, whereas the 55×55 window returns a higher abundance's estimate as well as comparable abundances between these detectors. For this reason, in what follows, we select a background window of 55×55 pixels.

The detection performance is assessed in terms of false alarm rate.⁶ Table IV shows the false alarm rate achieved for the three detectors. From this analysis, we note that the false alarm rate of

⁵Notice that the estimates provided by Kelly's GLRT, AMF, and ACE share the same value.

⁶Specifically, we repeat the same analysis conducted in [12], where the false alarm rate is evaluated as the number of no target pixels having their detector's statistic strictly higher than the one calculated using P_3 .

TABLE V
FALSE ALARM RATE FOR BOTH HEURISTIC AND CONSTRAINED APPROACHES
OVER W_1 AND W_2 WINDOWS APPLYING TWO CONFIGURATIONS
OF THE SPECTRAL MATRIX

Window	$\bar{\mathbf{T}}$	\mathbf{T}
W_1	Heuristic: 0.907%	Heuristic: 1.133%
	Constrained: 1.133%	Constrained: 1.133%
W_2	Heuristic: 5.895%	Heuristic: 6.122%
	Constrained: 6.122%	Constrained: 6.122%

the heuristic and the constrained detectors are almost the same and both lower than that of the considered competitors.

2) *Multiple Sub-Pixel Targets Detection*: In this subsection, we consider the target V_2 , a multiple target case as it is represented by the two spectral signatures: the cabin target V_{2c} (with signature \mathbf{t}_{2c}) and the back target V_{2b} (with signature \mathbf{t}_{2b}). Since for this scenario the ACUTE detector cannot be used, we will focus only on the results obtained through the heuristic and the constrained detectors and we use the ground truth from the dataset. As indicated by data description, the V_2 target is located at pixel coordinates $P_2 \equiv (353, 156)$.

At first, we focus on the abundances' estimation for this pixel P_2 . In this analysis, we consider two different configurations for the spectral matrix. Specifically, we take into account the spectral matrix already defined in the simulated scenario, i.e., $\mathbf{T} = [\mathbf{t}_{2c}, \mathbf{t}_{2b}, \mathbf{t}_3] \in \mathbb{R}^{116 \times 3}$, and the spectral matrix made by the two spectral signatures of the V_2 target only, i.e., $\bar{\mathbf{T}} = [\mathbf{t}_{2c}, \mathbf{t}_{2b}] \in \mathbb{R}^{116 \times 2}$. Around the PUT, the background window of size 55×55 pixels and the 3×3 pixels guard window are applied. Using both spectral matrices $\bar{\mathbf{T}}$ and \mathbf{T} , and inspecting the target abundance estimates for \mathbf{t}_{2c} and \mathbf{t}_{2b} , i.e., $\hat{\alpha}_{2c}$ and $\hat{\alpha}_{2b}$, respectively, we obtain low values for both algorithms. In particular, focusing on the V_{2c} target, the heuristic approach returns $\hat{\alpha}_{2c} \approx 0.094$, while the value obtained by means of the constrained approach is $\hat{\alpha}_{2c} \approx 0.024$. As for target V_{2b} , the estimated abundance is $\hat{\alpha}_{2b} \approx 0.006$ for the heuristic approach and zero for the constrained one. Even though the true abundance's values are not given in the dataset, the estimated abundances related to P_2 are low in spite of the claimed presence of V_2 in that pixel. This situation is probably due to possible mismatches between the real target signature and the presumed one.

In order to evaluate the detection performance in a multiple sub-pixel scenario, we consider the three test windows shown in Fig. 2, denoted by W_1 , W_2 , and W_3 , and of size 21×21 . Such windows are representative of different scenarios. Specifically, window W_1 is exactly centered where is located V_2 target, i.e., $P_{W_1} \equiv P_2 \equiv (353, 156)$, and is characterized by a mixed presence of vegetation and anthropic elements, such as roads, houses, and buildings. The second window, namely W_2 , is centered on pixel $P_{W_2} \equiv (275, 180)$ and it mainly encloses an urban area. Finally, the W_3 window, centered on pixel $P_{W_3} \equiv (200, 170)$, contains low vegetation. Given the most uniform coverage of W_3 , we assume that the pixels of this window represent background only. Therefore, we set the detection threshold over W_3 with $P_{fa} = 10^{-2}$. Specifically, the threshold value is estimated for each spectral matrix configuration, i.e., $\bar{\mathbf{T}}$ and \mathbf{T} , and both approaches. Table V summarizes the false alarm rates computed over the other two windows, namely, W_1 and W_2 . It is immediately evident that the false alarm rates for the heuristic and constrained approaches are of the same order for each test

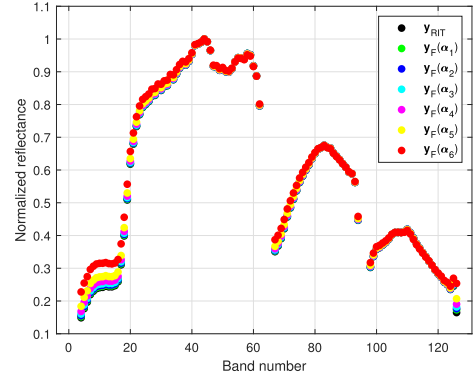


Fig. 9. Spectral reflectance normalized to the maximum value of the considered 116 spectral samples of filled pixel $P'_2 \equiv (240, 155)$. The filling strategy is applied according (34) and the background-target concentrations listed in Table VI.

window. Specifically, regardless of the spectral matrix applied, the false alarm rate is about 1% for W_1 window and is about 6% for the W_2 window. Notice that for the selected thresholds, target V_2 , which is present in W_1 , would not be detected. On the contrary, target V_3 , located at pixel $P_3 \equiv (282, 186)$, is within the W_2 window and a detection is obtained in its 3×3 pixels guard window, specifically at pixel with coordinates $(282, 185)$. Finally, it is worth noticing that the high number of false alarms in W_2 might be due to the presence of several anthropic elements.

To further investigate the behavior of the proposed detectors, we fictitiously introduce the V_2 target within a real pixel of the RIT dataset. Specifically, we identify a background pixel that corresponds to $P'_2 \equiv (240, 155)$, and according to the replacement model, we insert multi-target V_2 into the real pixel. Specifically, we denote by $\mathbf{y}_F(\alpha_n)$ the spectral reflectance values of the filled pixel, with n indicating a generic filling configuration corresponding to background values ranging from 0.6 to 0.1, and we define it as

$$\mathbf{y}_F(\alpha_n) = [\mathbf{t}_{2c}, \mathbf{t}_{2b}] \alpha_n + (1 - \alpha_n^T \mathbf{1}) \mathbf{y}_{RIT}, \quad (34)$$

where \mathbf{y}_{RIT} is the pixel reflectance of the RIT dataset, and $\alpha_n = [\alpha_{2c}, \alpha_{2b}]^T$ with α_{2c} and α_{2b} the abundances' values for V_{2c} and V_{2b} , respectively.

Particularly, we consider multiple configurations of background-target concentrations as shown by the values of α_n in Table VI: the concentrations of interest are set for background values from 0.6 to 0.1 and correspond to a cumulative target abundance in between 0.4 and 0.9, respectively. Fig. 9 shows the spectral reflectance of the filled pixel P'_2 for the different configurations of background-target concentrations.

Therefore, we process the filled pixel P'_2 in all the considered configurations for both the heuristic and constrained detectors using the spectral libraries $\bar{\mathbf{T}}$ and \mathbf{T} . In all these analyses, we verified that the output of detector is above its reference threshold, which means that the multiple sub-pixel target V_2 is correctly detected. Furthermore, Table VI shows the estimates of the concentrations of each component of the target V_2 , i.e., $\hat{\alpha}_{2c}$ and $\hat{\alpha}_{2b}$. From the table, we observe estimates for both the heuristic and constrained approaches very close to the true abundance values, especially for low background values. It is also important to remember that when using the three signatures' spectral matrix, also the abundance estimate of the third

TABLE VI
 ABUNDANCES' ESTIMATE OVER FILLED PIXEL P'_2 FOR DIFFERENT CONFIGURATIONS OF BACKGROUND-TARGET
 CONCENTRATIONS DEFINED ACCORDING TO (34). THE $\hat{\mathbf{T}}$ AND \mathbf{T} SPECTRAL MATRICES ARE APPLIED

$\alpha_n = [\alpha_{2c}, \alpha_{2b}]^T$		$(\hat{\alpha}_{2c}, \hat{\alpha}_{2b})$	$(\hat{\alpha}_{2c}, \hat{\alpha}_{2b}, \hat{\alpha}_3)$
$\alpha_1 = [0.35, 0.05]^T$	Heuristic	(0.237, 0.123)	(0.289, 0.038, 0.022)
	Constrained	(0.238, 0.114)	(0.292, 0.065, 0.000)
$\alpha_2 = [0.40, 0.10]^T$	Heuristic	(0.328, 0.132)	(0.263, 0.148, 0.039)
	Constrained	(0.279, 0.181)	(0.334, 0.130, 0.000)
$\alpha_3 = [0.45, 0.15]^T$	Heuristic	(0.367, 0.203)	(0.269, 0.196, 0.055)
	Constrained	(0.298, 0.270)	(0.379, 0.192, 0.000)
$\alpha_4 = [0.50, 0.20]^T$	Heuristic	(0.368, 0.312)	(0.398, 0.285, 0.000)
	Constrained	(0.359, 0.317)	(0.474, 0.204, 0.000)
$\alpha_5 = [0.55, 0.25]^T$	Heuristic	(0.465, 0.315)	(0.495, 0.267, 0.018)
	Constrained	(0.447, 0.336)	(0.561, 0.215, 0.007)
$\alpha_6 = [0.60, 0.30]^T$	Heuristic	(0.536, 0.354)	(0.580, 0.272, 0.038)
	Constrained	(0.536, 0.355)	(0.640, 0.223, 0.025)

endmember, i.e., t_3 , is provided. In this case, the values of $\hat{\alpha}_3$ are zero or negligible, as expected. Furthermore, the greater spectral library seems to not influence the estimation performance, at least for the analysed cases, obtaining results comparable to those of the two signatures' spectral matrix.

Finally, we conclude the assessment by summarizing the merits and drawbacks of the proposed methods. Starting from the computational requirements, the constrained method is more time-demanding since it requires to solve equation system (32) whereas the heuristic approach leads to a quadratic equation that admits easy closed-form solutions. This aspect is corroborated by the computation times measured in Subsection IV-A. However, the convergence curves highlight that, although both algorithms share the same behavior at the initial iteration values, the heuristic method is not guaranteed to approach the local stationary point as fast as the constrained solution due to the presence of a floor related to the likelihood variation. Nevertheless, both algorithms do not guarantee the convergence to the global stationary point. As for the detection performance, both methods share almost the same number of false alarms, whereas the heuristic detector returns P_d values higher than those related to the constrained detector for values of the abundances' sum lower than about 0.5. Notice also that the transition from low to high P_d values is sharper for the constrained method. From the estimation standpoint, the former returns more reliable values for the abundances than the latter and, more importantly, it is less inclined to estimate *false abundances* unlike the heuristic method that provides nonzero abundances for nonexistent signatures.

V. CONCLUSION

In this paper, we have addressed the detection of sub-pixel targets in hyperspectral images. As first step, we have introduced a generalization of the so-called replacement model that includes multiple spectral signatures with a constraint on the sum of their abundances. It is important to underline that such a model is different from the approximate additive model that is used by most of conventional algorithms. Then, under this generalized model, we have formulated the endmember detection problem as a binary hypothesis test and applied GLRT-like design criteria. Specifically, due to the intractable mathematics, we have suitably

modified the maximum likelihood approach to come up with cyclic estimation procedures. The first procedure heuristically incorporates the constraint on the abundances whereas the second approach exploits the Lagrange multiplier method. Finally, we have assessed their detection and estimation performance over synthetic and real-recorded data. As term of comparison, we have considered the so-called ACUTE detector proposed in [12], Kelly's GLRT, AMF, and ACE that, however, assume the presence of only one spectral signature in the pixel under test. The numerical examples have highlighted the effectiveness of both the proposed approaches with the detector based on the Lagrange multipliers overcoming the other counterparts.

Future research directions might encompass the design of detectors that assume the vector of the fill factors α is no longer deterministic but obeys a preassigned distribution based upon a priori information. In addition, model (1) can be further extended by considering adjacent pixels that could share some endmember signatures and, hence, can be jointly processed to detect such signatures.

APPENDIX A PROOF OF (17)

Let us consider the matrix argument of the determinant in (16) and observe that it can be written as

$$\left(\frac{1}{A}\mathbf{x} - \hat{\boldsymbol{\mu}}\right) \left(\frac{1}{A}\mathbf{x} - \hat{\boldsymbol{\mu}}\right)^T + \sum_{k=1}^K (\mathbf{z}_k - \hat{\boldsymbol{\mu}}) (\mathbf{z}_k - \hat{\boldsymbol{\mu}})^T \quad (35)$$

$$= \frac{1}{A^2} \mathbf{x} \mathbf{x}^T + (K+1) \hat{\boldsymbol{\mu}} \hat{\boldsymbol{\mu}}^T - \left(\frac{1}{A} \mathbf{x} + \tilde{\mathbf{z}}\right) \hat{\boldsymbol{\mu}}^T - \hat{\boldsymbol{\mu}} \left(\frac{1}{A} \mathbf{x} + \tilde{\mathbf{z}}\right)^T + \mathbf{Z} \mathbf{Z}^T \quad (36)$$

$$= \frac{1}{A^2} \mathbf{x} \mathbf{x}^T - (K+1) \hat{\boldsymbol{\mu}} \hat{\boldsymbol{\mu}}^T + \mathbf{Z} \mathbf{Z}^T \quad (37)$$

$$= \frac{1}{A^2} \mathbf{x} \mathbf{x}^T - \frac{1}{(K+1)} \left(\frac{1}{A} \mathbf{x} + \tilde{\mathbf{z}}\right) \left(\frac{1}{A} \mathbf{x} + \tilde{\mathbf{z}}\right)^T + \mathbf{Z} \mathbf{Z}^T = \frac{1}{A^2} \mathbf{x} \mathbf{x}^T + \mathbf{Z} \mathbf{Z}^T - \frac{1}{K+1} \frac{1}{A^2} \mathbf{x} \mathbf{x}^T - \frac{1}{K+1} \tilde{\mathbf{z}} \tilde{\mathbf{z}}^T \quad (38)$$

$$-\frac{1}{K+1} \frac{1}{A} \mathbf{x} \tilde{\mathbf{z}}^T - \frac{1}{K+1} \frac{1}{A} \tilde{\mathbf{z}} \mathbf{x}^T \quad (39)$$

$$= \left(\mathbf{Z}\mathbf{Z}^T - \frac{1}{K+1} \tilde{\mathbf{z}} \tilde{\mathbf{z}}^T \right) + \frac{K}{(K+1)} \frac{1}{A^2} \mathbf{x} \mathbf{x}^T - \frac{K}{K+1} \frac{1}{KA} \mathbf{x} \tilde{\mathbf{z}}^T - \frac{K}{K+1} \frac{1}{KA} \tilde{\mathbf{z}} \mathbf{x}^T \pm \frac{1}{K(K+1)} \tilde{\mathbf{z}} \tilde{\mathbf{z}}^T \quad (40)$$

$$= \mathbf{S}_1 + \frac{K}{K+1} \left(\frac{1}{A} \mathbf{x} - \frac{1}{K} \tilde{\mathbf{z}} \right) \left(\frac{1}{A} \mathbf{x} - \frac{1}{K} \tilde{\mathbf{z}} \right)^T, \quad (41)$$

where

$$\mathbf{S}_1 = \left(\mathbf{Z}\mathbf{Z}^T - \frac{1}{K+1} \tilde{\mathbf{z}} \tilde{\mathbf{z}}^T \right) - \frac{1}{K(K+1)} \tilde{\mathbf{z}} \tilde{\mathbf{z}}^T. \quad (42)$$

Exploiting the fact that $\det(\mathbf{I} + \mathbf{A}\mathbf{B}) = \det(\mathbf{I} + \mathbf{B}\mathbf{A})$, $\mathbf{A} \in \mathbb{C}^{N \times M}$ and $\mathbf{B} \in \mathbb{C}^{M \times N}$, we can write

$$\begin{aligned} & \det \left[\mathbf{S}_1 + \frac{K}{K+1} \left(\frac{1}{A} \mathbf{x} - \frac{1}{K} \tilde{\mathbf{z}} \right) \left(\frac{1}{A} \mathbf{x} - \frac{1}{K} \tilde{\mathbf{z}} \right)^T \right] \\ &= \det(\mathbf{S}_1) \\ & \times \det \left[\mathbf{I} + \frac{K}{K+1} \mathbf{S}_1^{-1/2} \left(\frac{1}{A} \mathbf{x} - \frac{1}{K} \tilde{\mathbf{z}} \right) \right. \\ & \left. \times \left(\frac{1}{A} \mathbf{x} - \frac{1}{K} \tilde{\mathbf{z}} \right)^T \mathbf{S}_1^{-1/2} \right] \\ &= \det(\mathbf{S}_1) \left[1 + \frac{K}{K+1} \left(\frac{1}{A} \mathbf{x} - \frac{1}{K} \tilde{\mathbf{z}} \right)^T \mathbf{S}_1^{-1} \left(\frac{1}{A} \mathbf{x} - \frac{1}{K} \tilde{\mathbf{z}} \right) \right] \end{aligned} \quad (43)$$

and the proof is complete.

REFERENCES

- [1] R. N. Patro, S. Subudhi, P. K. Biswal, and F. Dell'acqua, "A review of unsupervised band selection techniques: Land cover classification for hyperspectral earth observation data," *IEEE Geosci. Remote Sens. Mag.*, vol. 9, no. 3, pp. 72–111, Sep. 2021.
- [2] H. Zhai, H. Zhang, P. Li, and L. Zhang, "Hyperspectral image clustering: Current achievements and future lines," *IEEE Geosci. Remote Sens. Mag.*, vol. 9, no. 4, pp. 35–67, Dec. 2021.
- [3] N. Fiscante, P. Addabbo, F. Biondi, G. Giunta, and D. Orlando, "Unsupervised sparse unmixing of atmospheric trace gases from hyperspectral satellite data," *IEEE Geosci. Remote Sens. Lett.*, vol. 19, 2022, Art no. 6006405.
- [4] M. Shimoni, R. Haelterman, and C. Perneel, "Hyperspectral imaging for military and security applications: Combining myriad processing and sensing techniques," *IEEE Geosci. Remote Sens. Mag.*, vol. 7, no. 2, pp. 101–117, Jun. 2019.
- [5] N. Keshava and J. Mustard, "Spectral unmixing," *IEEE Signal Process. Mag.*, vol. 19, no. 1, pp. 44–57, Jan. 2002.
- [6] J. M. Bioucas-Dias et al., "Hyperspectral unmixing overview: Geometrical, statistical, and sparse regression-based approaches," *IEEE J. Sel. Topics Appl. Earth Observ. Remote Sens.*, vol. 5, no. 2, pp. 354–379, Apr. 2012.
- [7] N. M. Nasrabadi, "Hyperspectral target detection: An overview of current and future challenges," *IEEE Signal Process. Mag.*, vol. 31, no. 1, pp. 34–44, Jan. 2014.
- [8] D. Manolakis, E. Truslow, M. Pieper, T. Cooley, and M. Brueggeman, "Detection algorithms in hyperspectral imaging systems: An overview of practical algorithms," *IEEE Signal Process. Mag.*, vol. 31, no. 1, pp. 24–33, Jan. 2014.
- [9] H. Su, Z. Wu, H. Zhang, and Q. Du, "Hyperspectral anomaly detection: A survey," *IEEE Geosci. Remote Sens. Mag.*, vol. 10, no. 1, pp. 64–90, Mar. 2022.
- [10] D. Manolakis and G. Shaw, "Detection algorithms for hyperspectral imaging applications," *IEEE Signal Process. Mag.*, vol. 19, no. 1, pp. 29–43, Jan. 2002.
- [11] A. Schaum and A. Stocker, "Spectrally-selective target detection," in *Proc. Intl. Symp. Spectral Sens. Res.*, B. A. Mandel, Ed., 1997, vol. 12, pp. 2015–2018. [Online]. Available: <http://leupold.gis.usu.edu/docs/protected/procs/issr/1997/>
- [12] F. Vincent and O. Besson, "One-step generalized likelihood ratio test for subpixel target detection in hyperspectral imaging," *IEEE Trans. Geosci. Remote Sens.*, vol. 58, no. 6, pp. 4479–4489, Jun. 2020.
- [13] F. Vincent and O. Besson, "Target detection in hyperspectral imaging combining replacement and additive models," *Signal Process.*, vol. 188, 2021, Art. no. 108212. [Online]. Available: <https://www.sciencedirect.com/science/article/pii/S0165168421002504>
- [14] E. J. Kelly, "An adaptive detection algorithm," *IEEE Trans. Aerosp. Electron. Syst.*, vol. AES-22, no. 2, pp. 115–127, Mar. 1986.
- [15] E. J. Tentilucci and S. Adler-Golden, "Atmospheric compensation of hyperspectral data: An overview and review of in-scene and physics-based approaches," *IEEE Geosci. Remote Sens. Mag.*, vol. 7, no. 2, pp. 31–50, Jun. 2019.
- [16] D. Manolakis, R. Lockwood, T. Cooley, and J. Jacobson, "Is there a best hyperspectral detection algorithm?," in *Algorithms and Technologies for Multispectral, Hyperspectral, and Ultraspectral Imagery XV*, vol. 7334, S. S. Shen and P. E. Lewis, Eds. Bellingham, WA, USA: SPIE, 2009, pp. 13–28, doi: [10.1117/12.816917](https://doi.org/10.1117/12.816917).
- [17] H. Lütkepohl, *Handbook of Matrices*. Hoboken, NJ, USA: Wiley, 1997.
- [18] D. Snyder, J. Kerekes, I. Fairweather, R. Crabtree, J. Shive, and S. Hager, "Development of a web-based application to evaluate target finding algorithms," in *Proc. IEEE Int. Geosci. Remote Sens. Symp.*, 2008, pp. II-915–II-918.
- [19] M. Khoshboresh-Masouleh and M. Hasanlou, "Improving hyperspectral sub-pixel target detection in multiple target signatures using a revised replacement signal model," *Eur. J. Remote Sens.*, vol. 53, no. 1, pp. 316–330, 2020, doi: [10.1080/22797254.2020.1850179](https://doi.org/10.1080/22797254.2020.1850179).
- [20] T. D. Cocks, R. Janssen, A. E. Stewart, I. Wilson, and T. Shields, "The HyMap TM airborne hyperspectral sensor: The system, calibration and performance," in *Proc. 1st EARSeL Workshop Imag. Spectrosc.*, M. Schaeppman, D. Schläpfer, and K. I. Itten, Eds., Zurich, Paris, Oct. 6–8, 1998, pp. 37–42.
- [21] V. Roy, "Hybrid algorithm for hyperspectral target detection," *Proc. SPIE*, vol. 7695, 2010, Art. no. 769522, doi: [10.1117/12.849910](https://doi.org/10.1117/12.849910).
- [22] S. Khazai, A. Safari, B. Mojaradi, and S. Homayouni, "An approach for subpixel anomaly detection in hyperspectral images," *IEEE J. Sel. Topics Appl. Earth Observ. Remote Sens.*, vol. 6, no. 2, pp. 769–778, Apr. 2013.
- [23] U. Heiden, S. Roessner, K. Segl, and H. Kaufmann, "Analysis of spectral signatures of urban surfaces for their identification using hyperspectral HyMap data," in *Proc. IEEE/ISPRS Joint Workshop Remote Sens. Data Fusion over Urban Areas*, 2001, pp. 173–177.
- [24] F. C. Robey, D. R. Fuhrmann, E. J. Kelly, and R. Nitzberg, "A CFAR adaptive matched filter detector," *IEEE Trans. Aerosp. Electron. Syst.*, vol. 28, no. 1, pp. 208–216, Jan. 1992.
- [25] E. Conte, M. Lops, and G. Ricci, "Asymptotically optimum radar detection in compound-gaussian clutter," *IEEE Trans. Aerosp. Electron. Syst.*, vol. 31, no. 2, pp. 617–625, Apr. 1995.
- [26] S. Kraut and L. L. Scharf, "The CFAR adaptive subspace detector is a scale-invariant GLRT," *IEEE Trans. Signal Process.*, vol. 47, no. 9, pp. 2538–2541, Sep. 1999.



Pia Addabbo (Senior Member, IEEE) received the B.Sc. and M.Sc. degrees in telecommunication engineering, and the Ph.D. degree in information engineering from the Università degli Studi del Sannio, Benevento, Italy, in 2005, 2008, and 2012, respectively. She is currently an Associate Professor with the Giustino Fortunato University, Benevento, Italy. She is the coauthor of scientific publications in international journals and conferences. Her research interests include statistical signal processing applied to radar target recognition, global navigation satellite system reflectometry, and hyperspectral unmixing. She is currently an Associate Editor for the IEEE TRANSACTIONS ON SIGNAL PROCESSING, IEEE ACCESS, and Scientific Reports.



Nicomino Fiscante (Student Member, IEEE) was born in Benevento, Italy, on January 26, 1982. He received the M.Sc. degree (*cum laude*) in telecommunication engineering from the University of Sannio, Benevento, Italy, in 2007. From January to June 2007, he was trainee with the Antenna Group, The Netherlands Organization for Applied Scientific Research (TNO Defense, Security and Safety), The Hague, The Netherlands. From 2008 to 2012, he was with Mediterranean Agency for Remote Sensing and Environmental Control, Benevento, Italy. From 2012

to 2014, he was with Advanced Research Technology Spa, Passignano sul Trasimeno, Italy. Since 2014, he has been a Project Manager with Geoslab (now GeneGIS GI) and has increased numerous work experience both nationally and internationally thanks to the collaboration with important Companies, Research Centers, Universities and Institutions. His research interests include remote sensing, GIS, data processing, TLC and EM systems, mobile mapping systems, and renewable resources.



Gaetano Giunta (Senior Member, IEEE) received the degree in electronic engineering from the University of Pisa, Pisa, Italy, in 1985, and the Ph.D. degree in information and communication engineering from the University of Rome La Sapienza, Rome, Italy, in 1990. Since 1989, he has been a Research Fellow of the Signal Processing Laboratory, EPFL, Lausanne, Switzerland. In 1992, he became an Assistant Professor with the INFO-COM Department, University of Rome La Sapienza, Rome, Italy. From 2001 to 2005, he was with the Third University of Rome as an

Associate Professor, where he has been a Full Professor of telecommunications, since 2005. His research interests include signal processing for mobile communications, image communications, and security. He has been a Member of the IEEE Societies of Communications, Signal Processing, and Vehicular Technology. He was a Reviewer of several IEEE Transactions, IET (formerly IEE) proceedings, and EURASIP journals, and a TPC Member of several international conferences and symposia in the same fields.



Danilo Orlando (Senior Member, IEEE) was born in Gagliano del Capo, Italy, on August 9, 1978. He received the Dr. Eng. degree (with Hons.) in computer engineering and the Ph.D. degree (with maximum score) in information engineering from the University of Salento (formerly University of Lecce), Lecce, Italy, in 2004 and 2008, respectively. From July 2007 to July 2010, he was with the University of Cassino, Cassino, Italy, engaged in a research project on algorithms for track-before-detect of multiple targets in uncertain scenarios. From September to November

2009, he was a Visiting Scientist with the NATO Undersea Research Centre, La Spezia, Italy. From September 2011 to April 2015, he was with Elettronica S.p.A. engaged as System Analyst in the field of electronic warfare. In May 2015, he joined Università degli Studi "Niccolò Cusano", Rome, Italy, where he is currently an Associate Professor. In 2007, he has held visiting positions with the Department of Avionics and Systems, ENSICA (now Institut Supereur de l'Aeronautique et de l'Espace, ISAE), Toulouse, France, and from 2017 to 2019, with Chinese Academy of Science, Beijing, China. He is the author or coauthor of more than 170 scientific publications in international journals, conferences, and books. His main research interests include statistical signal processing with more emphasis on adaptive detection and tracking of multiple targets in multisensor scenarios. He was a Senior Area Editor of the IEEE TRANSACTIONS ON SIGNAL PROCESSING and is currently an Associate Editor for the IEEE OPEN JOURNAL ON SIGNAL PROCESSING, *EURASIP Journal on Advances in Signal Processing*, and *MDPI Remote Sensing*.



Giuseppe Ricci (Senior Member, IEEE) was born in Naples, Italy, in 1964. He received the Dr. and Ph.D. degrees in electronic engineering from the University of Naples Federico II, Naples, Italy, in 1990 and 1994, respectively. Since 1995, he has been with the University of Salento (formerly University of Lecce), Lecce, Italy, first as an Assistant Professor of telecommunications and since 2002 as a Professor. He held visiting positions with the University of Colorado, Boulder, CO, USA, from 1997 to 1998 and in April/May 2001, with Colorado State University, Fort

Collins, CO, USA, in July/September 2003, March 2005, September 2009, and March 2011, with Ensica, Toulouse, France, in March 2006, with the University of Connecticut, Storrs, CT, USA, in September 2008, and with the Arizona State University, Tempe, AZ, USA, from July to August 2019. His research interests include statistical signal processing with emphasis on radar processing, localization algorithms, and CDMA systems. From 2012 until 2016, he was a Member of the Multisensor Target Tracking Working Group, operating under the auspices of the International Society of Information Fusion, and from 2016 until 2021, he has been a Member of the Technical Area Committee in Signal Processing for Multisensor Systems of Eurasp. From February 2016 and June 2016, until April 2017, he was also a Rector Delegate for teaching activities and continuing education.



Silvia Liberata Ullo (Senior Member, IEEE) received the degree (*cum laude*) in electronic engineering from the University of Naples, Naples, Italy, in 1989, and the M.Sc. degree in management from the Massachusetts Institute of Technology, Cambridge, MA, USA, in 1992. Since 2018, she has been an Industry Liaison for IEEE Joint ComSoc/VTS Italy Chapter. From 2019 to 2021, she was the National Referent for FIDAPA BPW Italy Science and Technology Task Force. Since 2004, she has been a Researcher with the University of Sannio, Benevento,

Italy. She is a Component of the WG (Working Group) on Machine/Deep Learning for Image Analysis (WG-MIA) of IEEE GRSS IADF, the Image Analysis and Data Fusion Technical Committee (IADF TC) of the Geoscience and Remote Sensing Society. She is a Member of the Academic Senate and Ph.D. Professors Board. She is teaching courses in Electronic Engineering: Signal theory and elaboration, Telecommunication networks, Mathematics, for the Bachelor Program, Lab on Earth monitoring and mission analysis for the Master Program, Optical and radar remote sensing, for Ph.D. students. She has authored more than 80 research papers, coauthored many book chapters. Her research interests include signal processing, radar systems, sensor networks, remote sensing, satellite data analysis, machine learning, and quantum ML. She is the Editor of two books. She is an Associate Editor for relevant journals and the Guest Editor of many special issues. She worked in the private and public sectors from 1992 to 2004, before joining the University of Sannio. Before the M.Sc. degree, she was the recipient of an ITALTEL scholarship in 1990.